AIAA JOURNAL
Vol. 47, No. 3, March 2009

Dynamics of Plumes Generated by Local Injection of Ablated Material

Alex Povitsky* and Kedar Pathak†
University of Akron, Akron, Ohio 44325-3903
and
Datta Gaitonde‡
U.S. Air Force Research Laboratory, Wright–Patterson Air Force Base, Ohio 45433

DOI: 10.2514/1.38126

Numerical modeling is employed to study the heat transfer modulation between the thermal protection shield and the gas flow that is caused by ejection of underexpanded pyrolysis gases through the cracks in the thermal protection shield. The simulations are performed for an axisymmetric bluff body flying at Mach 7. The influence of the geometry of the thermal protection shield on the heat transfer pattern is studied for two representative shapes. The results are presented for three different flight altitudes (low, ground level; moderate, 20 km; and high, 30 km). At the low altitude, the plume pressure is lower than the pressure behind the detached front shock wave and the plume propagates slowly along the wall surface. At high and moderate altitudes, the plume path (and, consequently, the convective heat transfer between the thermal protection shield and the plume) depends on the plume interaction with the bow shock wave. The effect of viscosity for the plume injection conditions and freestream Mach number considered is found to be negligible at simulated altitudes. The effect of the initial pressure of pyrolysis gas on the plume dynamics is significant. The presence of the blast wave associated with the underexpanded plume alters the heat transfer and increases mixing. Finally, the enhanced heat transfer caused by the emergence of multiple plumes is investigated.

Nomenclature

E	=	total energy per unit mass
g	=	vector of fluxes in the radial direction
l_{visc}	=	viscous length scale, $\sqrt{\upsilon t}$
M	=	Mach number
p	=	pressure
Q	=	heat flux
Q_0	=	normalization parameter for heat flux
T_{NW}	=	temperature at the point located at the distance of one grid step to the wall
T_W	=	temperature at the wall surface
t	=	time
u	=	axial velocity
v	=	radial velocity
w	=	vector of fluxes in the axial direction
x	=	axial coordinate
y	=	radial coordinate
υ	=	kinematic viscosity

I. Introduction

EXTENSIVE research has been conducted in predicting the ablation rates of a thermal protective shield (TPS) due to hypersonic flow around aerospace vehicles. When subjected to increasing heat flux or temperature, thermal protection materials may pyrolize and/or ablate. Pyrolysis is chemical decomposition in the interior of a TPS material, which releases gaseous by-products without consuming atmospheric species. Ablation is a combination of vaporization, sublimation, and reactions (such as oxidation) that convert solid surface species into gaseous species [1]. The majority of published ablation and pyrolysis studies are limited to the setup of uniformly distributed ablated mass flux that varies gradually along the TPS surface and does not cause separation of the boundary layer.

Local nonuniform ablation can produce local plumes having much higher pressure, injection speed, and density compared with those corresponding to the average ablation speed under the same flight conditions. The severely underexpanded gas escapes through the cracks as a series of high-pressure plumes. Small-scale but high-intensity phenomena such as locally nonuniform mass transfer across the TPS surface can greatly affect the overall flowfield about the vehicle, heat exchange between the gas surrounding the vehicle and the TPS surface, and the overall ablation and pyrolysis rates. Escape of pyrolysis gases dramatically changes the surface temperature and can trigger transition to turbulence [2]. Previous studies regarding transition to turbulence caused by pyrolysis are based on uniform diffusion of the produced gas through micropores of the scale of TPS fiber thickness and not through macrocracks resulting from spallation [3–5]. One reason for nonuniform ablation is impingement of solid objects such as debris, ice, and/or foam into TPS elements [6]. Another reason is the formation of cracks and gas escape routes because of the nature of TPS materials at high temperature. The current study is aimed at modeling of the heat transfer modulation caused by the local plume(s) emergence through macrocracks for the range of flight altitude, initial plume pressure, and the shape of the TPS. The fluid dynamics of the plume are much more involved compared with the extensively studied jet-in-crossflow setup because of 1) interaction of pyrolysis plume with the detached bow shock wave in hypersonic flight and 2) enhanced mixing of plume with surrounding gas because of the pressure wave associated with the underexpanded plume.

Emerging plumes can alter the pressure gradient and the shape of velocity profile around the TPS, causing formation of a separation vortex with enhanced convective heat transfer from the high-speed flow to the TPS. On one hand, intense cooling from pyrolysis gases may increase thermal stresses and enhance spallation. On the other hand, in principle, pyrolysis gases can be used for desired cooling of

Presented as Paper 0577 at the the 46th AIAA Aerospace Sciences Meeting and Exhibit, Reno, NV, 6–10 January 2008; received 17 April 2008; revision received 5 November 2008; accepted for publication 14 November 2008.

*Associate Professor, Department of Mechanical Engineering. Member AIAA.
†Graduate Research Assistant, Department of Mechanical Engineering.
‡Technical Area Leader, High-Speed Flows, Air Vehicles Directorate, 2210 Eighth Street. Fellow AIAA.

the TPS if their escape routes are properly organized. Overall, the local heat- and mass- transfer processes will be greatly amplified in comparison with those in the laminar boundary layer of regular ablation. Modeling and scaling of these phenomena are future steps in the current research that will map out the uncharted regimes beyond spatially homogeneous ablation.

The pyrolysis gas of carbon-phenolic TPS can be approximately considered a mixture of H, H_2, CO, and CH_4 [7]. The temperature of pyrolysis gas ranges from 800 K at the inner surface to 1800 K at the outer surface of the pyrolysis zone, based on flight thermocouple data for Pioneer-Venus [7]. Pyrolysis gas pressure inside the TPS of Pioneer-Venus is between 8 and 30 atm for the four Venus vehicles (see [7]). Such a high internal pressure in the pyrolysis layer induces spallation. The observed rough surface with deep cracks in TPS confirms the importance of the modeling of nonuniform ablation. References [8,9] show a view of millimeter-scale cracks in a charring ablator observed with the von Karman Institute for Fluid Dynamics (VKI) Plasmatron. The typical thickness of cracks that appear because of intensive heating is of the order of millimeters [8,9], and this size was adopted in the current study.

In a broader sense, the size of the initial plume diameter ranges from microns to centimeters, depending on whether the ablated gas escapes through the pores in the TPS material or its ablation is caused by mechanical damage. In a composite, the space scales range from individual fiber diameter (7 μm) to the apparent diameter of tows and warps (300–500 μm) [10–12]. At the limit of small scales of cracks, carbon–carbon composites can generally contain a significant initial amount of cracks, voids, and debonded fiber/matrix interfaces, which can yield a porosity level as high as 20%. The typical size of cracks/voids is 14 μm and the size of debonded interfacial gaps is 0.5 μm [13]. On the other hand, the mechanical damage to the TPS may cause formation of much larger local intense ablation spots in the TPS [14].

In this paper, the recently developed methodology for modeling for laser ablation [15,16] is adapted to obtain physical understanding of the dynamics of pyrolysis gases on ablators. The paper is organized as follows. In Sec. II, the configuration, mathematical model, and numerical method used are described. In Sec. III, the effect of flight altitude on the plume dynamics and heat transfer is discussed. In Sec. IV, the role of initial pressure of pyrolysis gases is investigated. The injection of multiple pulses is presented in Sec. V. In Sec. VI, the influence of the shape of the TPS on the plume interactions is obtained.

II. Description of Model

A. Conditions of Flight and Emerging Plume

The axisymmetric ellipsoid bluff TPS shape chosen for this study is shown in Fig. 1. The plume emergence for the TPS shape considered in [17] is studied in Sec. VI. The Mach number of flight for the current study is $M = 7$. For this Mach number, a detached bow shock wave exists, as seen in Fig. 2a.

Parameters of the atmosphere for different altitudes that are being investigated are presented in Table 1. The initial temperature of the TPS is assumed to be equal to the surrounding air temperature at all altitudes. This temperature is an aftershock temperature for respective altitude, as given in Table 1.

The initial conditions of injected pyrolysis gas are given in Table 2 (see [7]). The pyrolysis gas pressure inside the TPS may vary between 8 and 30 atm. It is assumed that the pyrolysis pressure inside the TPS is independent of the choked pressure at the TPS surface, and the initial plume pressure is assumed to be equal to 30 atm unless specified otherwise. The temperature of pyrolysis gas ranges from 800 K at the inner surface to 1800 K at the outer surface of pyrolysis zone. The initial temperature of plume injection is assumed to be equal to 1000 K in the current study. The duration of an individual plume injection is assumed to be equal to 5 ms.

The heat transfer is evaluated by the difference between the initial TPS surface temperature and the convected plume temperature near the TPS surface (see Sec. II.C).

B. Governing Equations and the Numerical Method

The developed model is based on the compressible two-species Euler and Navier–Stokes equations. A similar model has recently been applied to the modeling of multiple-spot laser ablation [18]. The Euler equations in 2-D axisymmetric coordinates (x, y) (see Fig. 1) are given by

$$\frac{\partial \sigma}{\partial t} + \frac{\partial w}{\partial x} + \frac{\partial g}{\partial y} = s \tag{1}$$

where the vectors of conserved variables and fluxes are given by

$$\sigma = (\rho, \rho u, \rho v, E) \qquad w = (\rho u, p + \rho u^2, \rho uv, (\rho E + p)u)$$
$$g = (\rho v, \rho uv, p + \rho v^2, (\rho E + p)v)$$
$$s = -(\rho v/y, \rho uv/y, \rho v^2/y, (\rho E + p)v/y)$$

Variables ρ, u, v, and E represent density, axial velocity, radial velocity, and total energy per unit mass, respectively. The latter quantity is defined as

$$E = \frac{p}{(\gamma - 1)\rho} + \frac{1}{2}(u^2 + v^2) \tag{2}$$

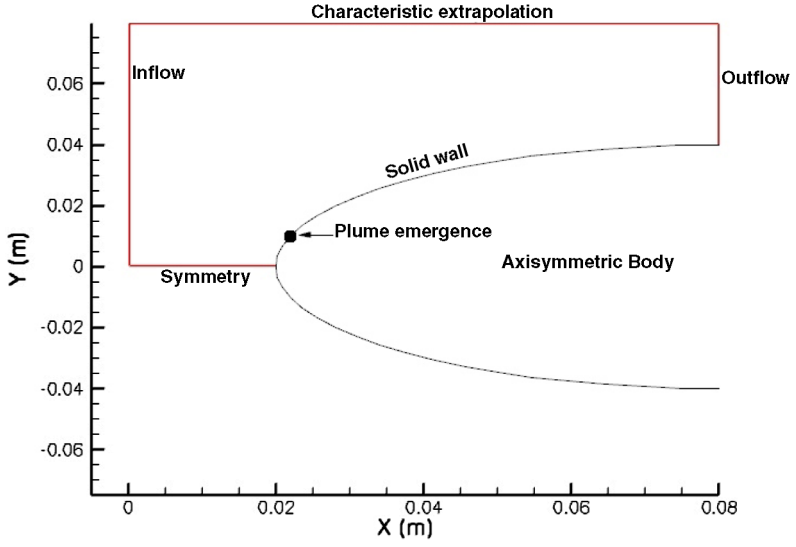

Fig. 1 Schematic of the problem showing the shape of the representative TPS and computational domain.

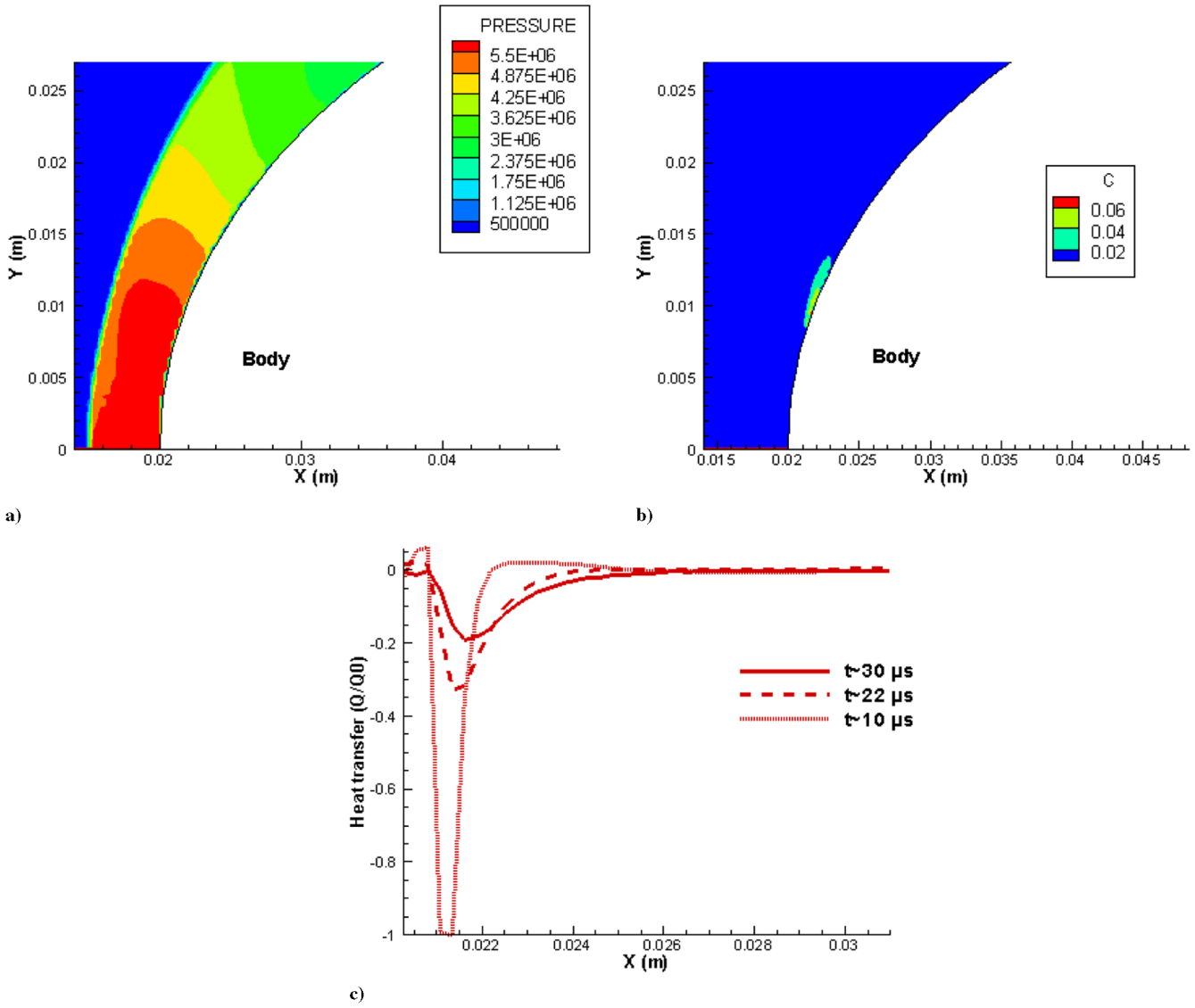

Fig. 2 For flight at the ground level: a) pressure distribution, b) plume concentration, and c) heat transfer at the TPS wall.

The ratio of specific heats γ for inviscid fluid satisfies the following equation:

$$\frac{\partial \gamma}{\partial t} + \frac{\partial \gamma u}{\partial x} + \frac{\partial \gamma v}{\partial y} = -\frac{\gamma v}{y} \tag{3}$$

The variable γ is used in the current study to show the plume boundary and plume pattern [19].

The method employed by Quirk and Karni [20] is adopted to evaluate the influence of viscous stresses. The effective viscous length scale can be defined as

$$l_{\text{visc}} = \sqrt{\upsilon \tau} \tag{4}$$

where υ is viscosity and τ is the time scale. This criterion is based on the analytical solution for the penetration of boundary layer into the fluid at rest due to the impulsive motion of the plate. If the viscous length scale is 2–3 orders of magnitude smaller than the plume diameter, the dynamics of plumes can be described by the compressible inviscid Euler conservation equations for mass, momentum, and energy [21]. Comparison of viscous and inviscid solutions for plume dynamics, presented in Sec. II.D, confirms the inviscid simplification of governing equations.

The numerical method used to solve gas dynamics equations is the first-order-accurate Godunov method using uniform numerical grid. The survey of numerical methods useful for such simulations can be found in the earlier work by Pathak and Povitsky [22,23]. In the study [23], the choice of the first-order-accurate Godunov method from several other available methods is validated for highly underexpanded plumes. The accuracy of the code was tested and verified using the Sedov–Taylor explosion problem [19]. A typical mesh employs 300×300 points. Simulations for the considered

Table 1 Flight regimes and gas parameters before and after the bow shock wave at $Ma = 7$

Flight altitude, km	Parameters of surrounding gas before and after the bow shock wave, respectively						Flight velocity, m/s
	Pressure, atm		Temperature, K		Density, kg/m^3		
0 (ground)	1	58	288	3055	1.2	6.61	2381
20	0.08	4.64	217	2302	0.12	0.71	2066
30	0.01	0.58	233	2472	0.01	0.08	2141

Table 2 Plume injection parameters

Parameter	Value
Pressure	30 atm
Temperature	1000 K
Density	10.45 kg/m^3
Velocity	400 m/s
Spot size	6 mm
Time of injection	5 μs

problem have been done with different meshes and results obtained on the 150×150 mesh are similar to those obtained on the 300×300 mesh.

C. Plume Emergence and Heat Transfer for Flight at Ground Level

The flight at ground level is taken as a baseline case. Figure 1 shows the simulated body covered with the TPS, together with the computational domain and boundary conditions. The plume emergence point is taken to be a few grid cells above the stagnation point. Each case is modeled by calculating the flowfield for steady flight at a corresponding altitude of flight before emergence of the plume. The distribution of pressure for steady flight is shown in Fig. 2a. The computed plume concentration is shown in Fig. 2b, and a heat transfer at the TPS wall for the flight at the ground level is shown in Fig. 2c. A detached shock is evident, which is important in the heat transfer mechanism between the plume and the TPS (see Fig. 2a).

Governing equations (1) are solved using 1) isothermal and 2) adiabatic boundary conditions at the TPS surface. For the former case, the local TPS wall temperature is equal to that for the steady flight. For the latter case, the TPS wall flux is assumed to be equal to zero. For both cases, the intensity of heat transfer between the plume and the TPS is estimated by

$$\Delta T = T_{NW} - T_W \tag{5}$$

where T_W is the TPS temperature for the steady flight before the emergence of the plume and T_{NW} is the gas temperature at the point located at the distance Δn (equal to the grid step) in the normal direction to the TPS at the time moment t after the plume emergence. The TPS surface is curvilinear, and so the T_{NW} is determined by the interpolation of temperature values at neighboring grid points. For adiabatic heat flux, the value of T_{NW} is taken at the current time moment, whereas the value of T_W is taken for the steady flight before emergence of plume. The value of ΔT is positive if heating of the TPS surface occurs, and it is negative if the plume cools the TPS surface. The estimates of heat flux $Q = K\Delta T/\Delta n$ at the TPS surface are listed in Table 3 for various cases to be considered. As shown in Table 3, the heat fluxes for adiabatic and isothermal (last row in Table 3) cases at 20 km of altitude of flight appear to be very close to each other, and therefore the adiabatic heat flux estimate is used in the current study. The x coordinate of the maximum heat transfer is shown in Table 3.

The normalization heat flux Q_0 is chosen as the value of $K\Delta T/\Delta n$ obtained at $t = 10$ μs, which is the estimate of the maximum absolute value of heat flux at all selected time moments for all altitudes. The values of normalized Q/Q_0 are presented in the subsequent discussion.

In this study, the estimation of heat flux is done in two ways: with and without considering the variation of thermal conductivity K with temperature. The curve fit for thermal conductivity is acquired from [24]:

$$K(T) = 1.5207 \times 10^{-11} \times T^3 - 4.8574 \times 10^{-08} \times T^2 + 1.0184 \times 10^{-04} \times T - 3.9333 \times 10^{-04} \text{ W/(mK)} \tag{6}$$

In principle, more elaborate curve fits exist for evaluating the value of K (see [25] and references therein). The preceding simple curve fit for K is chosen here to evaluate its effect on heat flux with temperature, which appears to be modest. The heat flux is calculated as

$$Q = K\frac{\partial T}{\partial n} \tag{7}$$

where the thermal conductivity being the function of temperature is evaluated as

$$K = K\left(\frac{T_{nw} + T_w}{2}\right)$$

including its value at 10 μs, and $K_0 = K(T(t = 10\ \mu))$. The normalized heat flux Q/Q_0 calculated considering the variation of thermal conductivity is different by a fraction K/K_0 from the Q/Q_0 calculated without considering this variation. It is found that differences in Q/Q_0 calculated in these two ways are small, which is reported in Sec. III for the case of heat transfer at 20 km.

The pressure on ground level behind the shock wave (Fig. 2a) is larger than the initial plume pressure. Consequently, the plume does not depart from the wall or traverse into the domain. The plume remains attached to the TPS wall and it is dragged with the flow along the wall (see Fig. 2b). It can be seen that the heat transfer attains its peak in the vicinity of plume emergence that is caused by the initial cold temperature of the plume. At ground level, the heat transfer due to the plume convection at the TPS surface is weak (see Fig. 2c) because the high pressure does not allow the mushroom-type plume pattern (that is observed for higher altitudes and will be discussed later in the study) to be formed. Therefore, the magnitude of heat flux shown in Fig. 2c decreases rapidly as the plume is convected. The plume being attached to and dragged along the wall is observed for the altitude of flight up until a few kilometers from the ground. Hence, the preceding described heat transfer pattern remains almost the same for the first few kilometers from the ground. When the altitude approaches 20 km, the plume leaves the surface and forms a mushroom pattern, which is discussed in the following sections.

Compared with higher altitudes, the convection of plume along the TPS is slow, because the plume remains in the low-speed near-wall area. At $t \sim 10$ μs in Fig. 2c, some positive heat transfer area is observed upstream and downstream of the negative peak. This is due to the relatively low pressure of plume that draws in the surrounding hot flow near the stagnation point.

The heat transfer between gas and TPS is characterized by temperatures of gas, TPS surface, and pyrolysis gas $T_g > T_W > T_{\text{pyr}}$, and the cooling effect of the TPS surface by escaping pyrolysis gas can be compared with the heating effect by the surrounding gas. According to [26], the steady-state convective heat flux at the stagnation point for a cold nonablating TPS wall is given by the Sutton–Graves formula:

$$q_{\text{conv}} = 1.74153 \times 10^{-4}\sqrt{\frac{\rho}{r}}V^3 \tag{8}$$

Table 3 TPS wall heat flux at different altitudes; $Q = K(\partial T/\partial n)$

	Location of peak along the wall X (m) at different time moments			Magnitude of peak (MW/m^2) at different time moments		
Altitude, km	$t \sim 10$ μs	$t \sim 22$ μs	$t \sim 30$ μs	$t \sim 10$ μs	$t \sim 22$ μs	$t \sim 30$ μs
0	.0213	.0213	.0216	0.2790	0.1047	.0750
20	.0216	.0251	.0265	0.5127	0.1331	0.1807
30	.0213	.0224	.0227	0.9245	0.8416	0.8771
20 (isothermal boundary condition)	.0216	.0251	.0265	0.5318	0.1388	0.1814

where q is convective heat flux (W/m^2), ρ is the air density (kg/m^3), r is the radius of the nose (m) (0.03 m in current computations), V is the flight speed (m/s), and the coefficient 1.74153×10^{-4} is for air. According to these formulas and the data of Table 1, the convective heat flux is 14.86 MW for ground elevation, 3.07 MW for 20 km of elevation, and 0.98 MW for 30 km of elevation. For ground-level flight and 20 km of elevation flight, the heat flux is larger than that of discrete plumes, whereas for 30 km of elevation flight, the fluxes are of the same order of magnitude (see Table 3).

Note that the preceding formulas have been obtained for a cold TPS wall at the stagnation point: that is, for conditions of maximum heat transfer between the surrounding gas and the TPS surface. Also, the wall-heating rate is significantly reduced by uniform ablation, because a surface blowing velocity is produced [1]. In addition, the nose radius of air vehicles may be larger than 0.03 m. Therefore, the cooling heat transfer introduced by discrete plumes is comparable with the steady heating heat transfer from the surrounding gas to the TPS surface.

D. Comparison of Viscous and Inviscid Formulations for Plume Dynamics

To examine the importance of viscous momentum transfer, the plume patterns and heat transfer at 20 km are obtained by solving the inviscid Euler and viscous Navier–Stokes equations (see Fig. 3). Note that in this and subsequent figures, the plume fluid is distinguished by visualizing γ, the ratio of specific heats. The difference between computational results obtained by the two approaches is minor, because the initial size of the ablative plume spot is 6 mm, whereas the boundary-layer thickness is of the submillimeter scale. In addition, the velocity and pressure of plume injection is 1 order of magnitude higher than the corresponding values of surrounding flow in the boundary layer. Thus, the plume is developing beyond the near-wall boundary layer. There is no significant difference in the plume pattern for these two formulations; hence, further simulations are performed using the Euler equations because of the lesser amount of required computational time. The peaks in heat transfer at the TPS wall (see Figs. 3c and 3d) are similar for inviscid and viscous formulations.

III. Effect of the Flight Altitude on Plume Dynamics and Heat Transfer

Figure 4 shows the plume concentrations as the plume evolves at 20 km. The emergence of plume creates the nonuniformity in the flow behind the shock wave. At 20 km, the bow shock wave remains strong (see Table 1 for pressures before and after the shock wave) and the postshock flow can be altered only temporarily by the single plume emergence. The plume core bends initially because the flow accelerates through it along the surface of the TPS. At later time moments, the acceleration of flow between the detached front shock wave and the TPS is almost uniform across the plume, as seen from the vector field in Figs. 4a and 4b. This turns the kidney-shaped

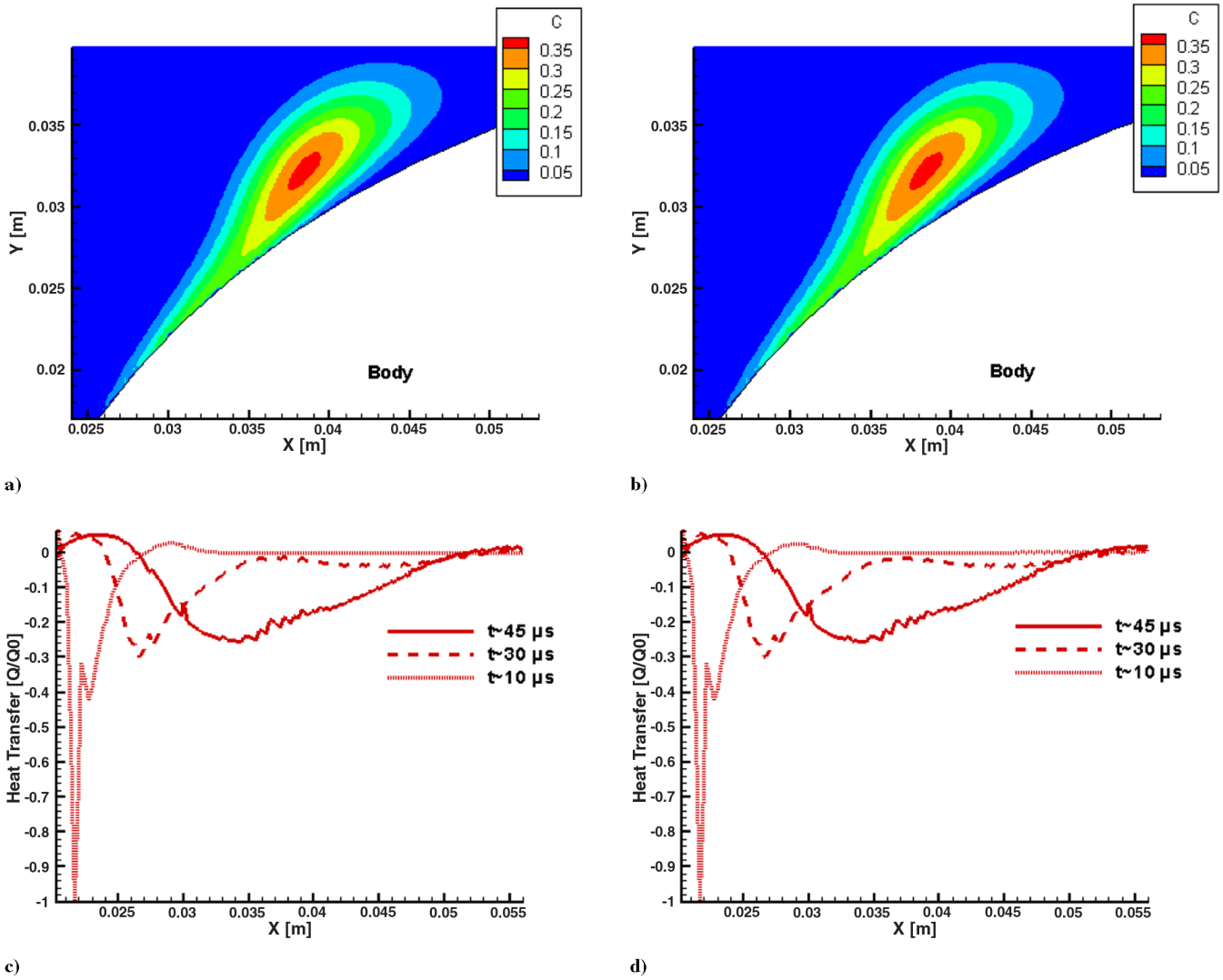

Fig. 3 Comparison of viscous and inviscid models for flight at the altitude of 20 km at $t \sim 45$ μs: a) plume concentration obtained with Euler equations, b) plume concentration obtained with Navier–Stokes equations, c) heat transfer coefficient obtained by the inviscid model, and d) heat transfer coefficient obtained by the viscous model.

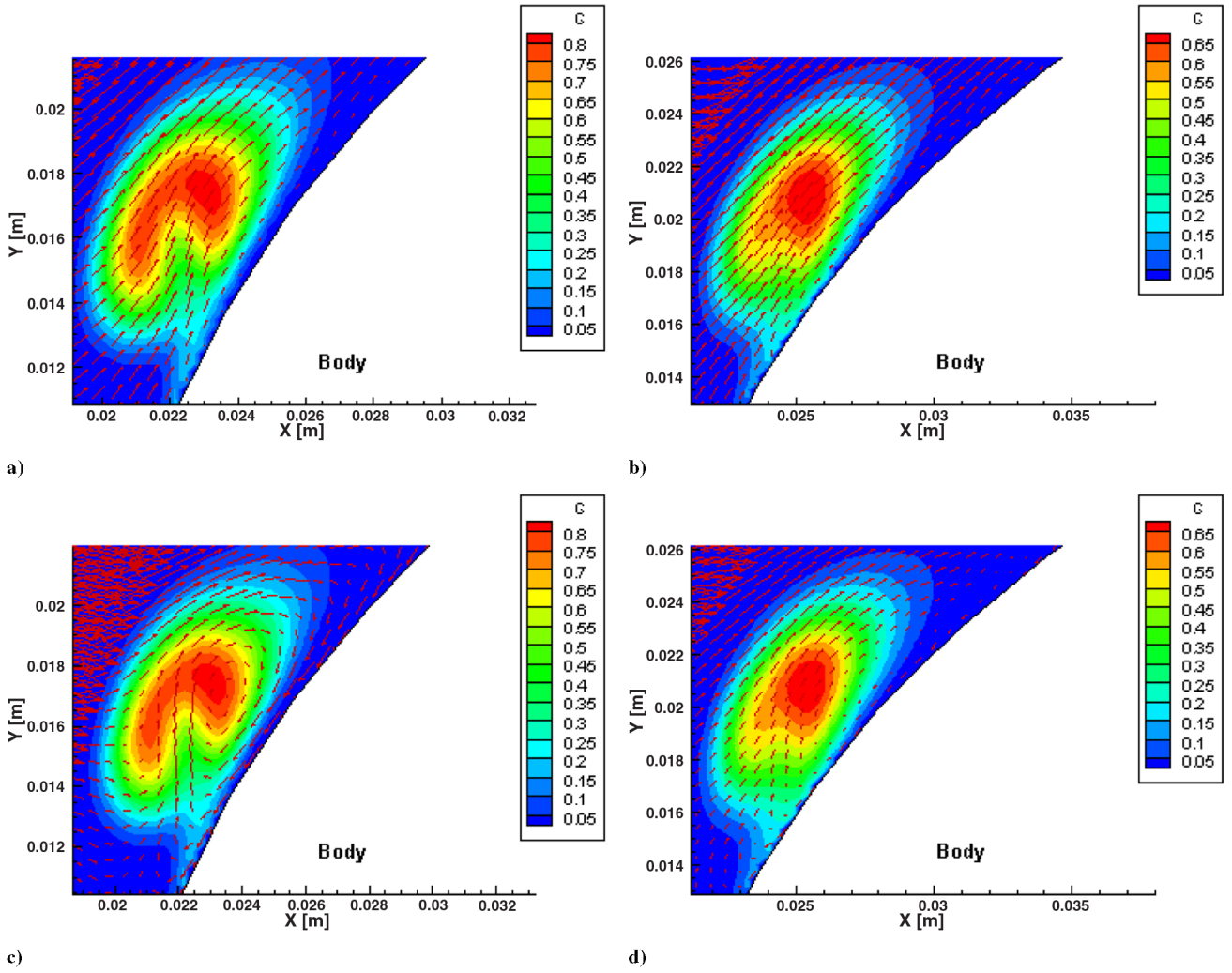

Fig. 4 Plume concentration and flow velocity at flight altitude of 20 km: a) original velocity vector field at $t \sim 20$ μs, b) original velocity vector field at $t \sim 25$ μs, c) modified vector field $\mathbf{V} - \mathbf{V}_{\text{ref}}$ at $t \sim 20$ μs, and d) modified vector field, $\mathbf{V} - \mathbf{V}_{\text{ref}}$ at $t \sim 25$ μs.

plume core formed by two vortices into an oval structure (see Figs. 4c and 4d). In Figs. 4c and 4d, the vector field is modified by subtracting a velocity $\mathbf{V}_{\text{ref}}$ at the approximate core center of the plumes. The shape is a typical Kelvin oval formed by letting the stream flow normal to the vortex pair. This plume shape is then maintained throughout its course over the body.

In terms of plume density, at $t \sim 20$ μs (Fig. 5a) the high-density area in the flowfield is a narrow kidney-shaped region of plume. This region is scattered after a few microseconds and turns into an oval, as shown in Fig. 5b. Note that the area of the oval is larger than the area of the kidney-shaped plume and the density of the plume material is smaller (compare Figs. 5a and 5b). The temperature of the oval-shaped plume becomes closer to the temperature of the surrounding gas. In the current conditions, the temperature of the oval plume becomes larger than the initial temperature of the plume [which is maintained for the kidney-shaped plume (compare Figs. 5c and 5d)]. As a result, the cooling effect of the plume is softened.

The temporarily disturbed flowfield behind the front shock wave is restored between 20 and 25 μs (see Fig. 5b). This gives the uniform acceleration across the plume, turning the core into an oval, as discussed previously. In other words, the detached front shock wave smoothes any nonuniformity in the flow behind the shock wave at the altitude of 20 km.

The interaction of shock wave and injection pressure wave affects the heat transfer to the body by altering the temperature field around the body. The pressure wave associated with the plume and raising the gas temperature is shown in Fig. 6a. The high temperature is attained near the stagnation point, because the hot gases are entrained by the plume that affects the heat transfer at the TPS surface. Therefore, the positive heat transfer is observed around the stagnation region [$x \sim 0.02$ m (see Figs. 6b and 7d)].

In the later moments, the heat transfer is the maximum near the plume tail when the plume is pushed back to the body by the bow shock wave, as explained subsequently. It can be seen at $t \sim 30$ μs that the area with positive heat transfer around the stagnation region is larger than that at $t \sim 22$ μs.

In Fig. 7, the plume concentration and the heat transfer are shown at the corresponding time moments at the altitude of flight of 20 km. The heat transfer is the maximum [$t \sim 10$ μs (see Fig. 7d)] at the location of plume emergence in the initial stage of plume evolution. At later time moments, the cooling heat transfer reaches its maximum near the plume tail when it touches the TPS wall. It should be noted that the peak in heat transfer is higher at $t \sim 30$ μs than that at $t \sim 22$ μs. This occurs because the detached bow shock wave, which was distorted by the plume injection, restores and pushes the plume toward the wall. Heat transfer at this altitude is evaluated for both cases, with and without the variation of thermal conductivity, and it can be seen that the heat transfer resulting with these two formulations is very similar.

At the higher altitude of 30 km, the evolved plume is shown in Fig. 8a. In this case, the strength of shock wave is low in terms of pressure difference across the shock wave (see Table 1), and hence the plume is able to penetrate through the shock wave, as shown in Fig. 8b. The emergence of plume distorts the shock wave to a much larger extent at higher altitudes (see Fig. 8a). The plume remains detached from the TPS and maintains its kidney shape for a longer time, as can be seen in Fig. 8.

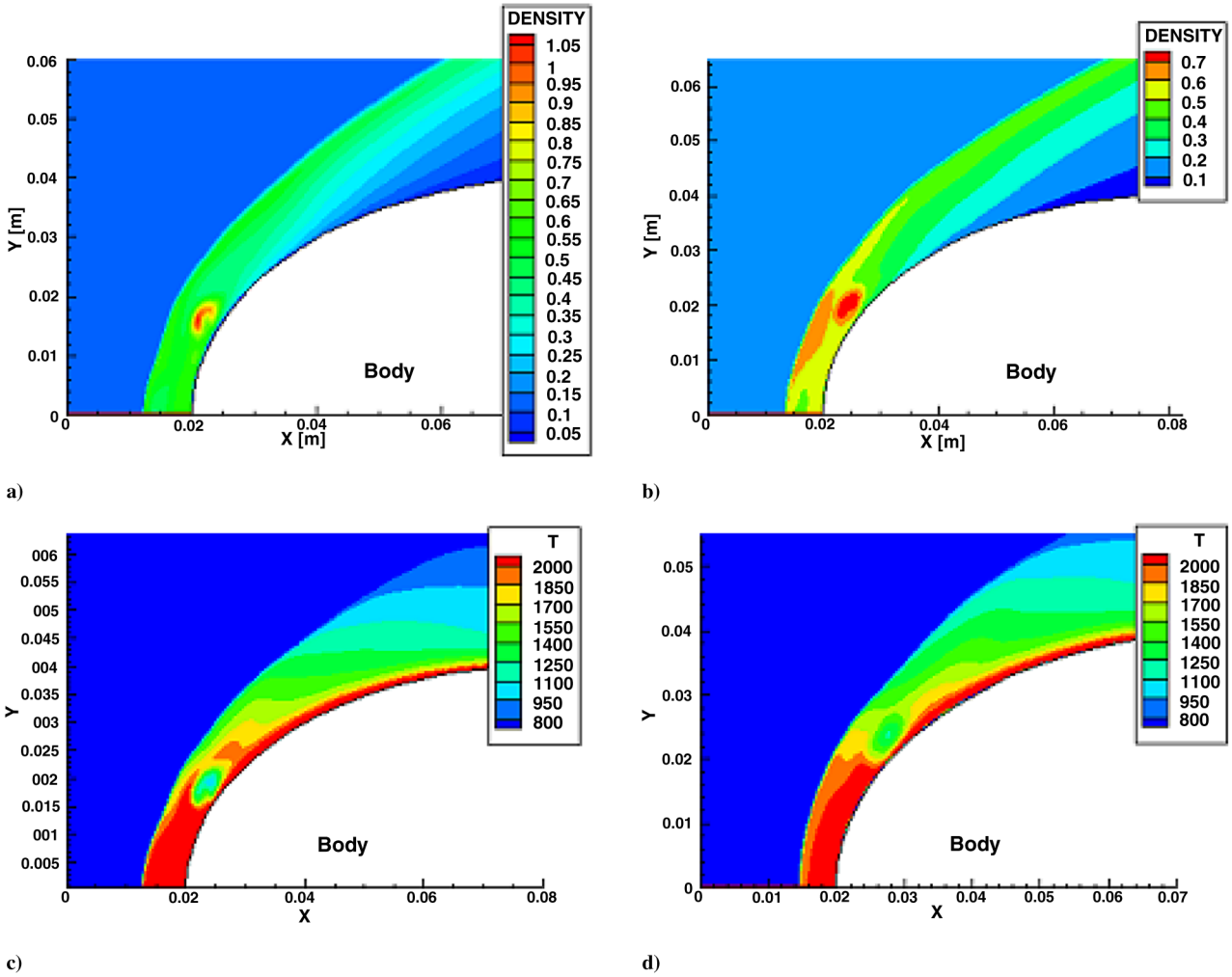

Fig. 5 Plume density and temperature: a) density at $t \sim 20$ μs, b) density at $t \sim 25$ μs, c) temperature at $t \sim 20$ μs, and d) temperature at $t \sim 25$ μs.

The heat transfer for the altitude of flight of 30 km is shown in Fig. 9b. At 30 km, the heat transfer due to the plume convection decreases with time, as the plume stays away from the wall on account of its initial high pressure (see Fig. 8). The cooling effect is caused by the interaction of the right lobe of the kidney-shaped plume with the TPS wall, as shown in Fig. 8b. The temperature of the kidney-shaped plume is smaller than that for the oval plume (see the discussion in the beginning of this section); therefore, the cooling effect is more significant than that at the altitude of flight of 20 km. The positive maxima seen in the heat transfer graphs (Fig. 9b) are caused by the outgoing pressure associated with the underexpanded plume (see Fig. 6). Unlike at the lower flight altitude of 20 km, these peaks are clearly seen downstream of the plume. In addition, there is the interaction of the plume-associated pressure wave with the front

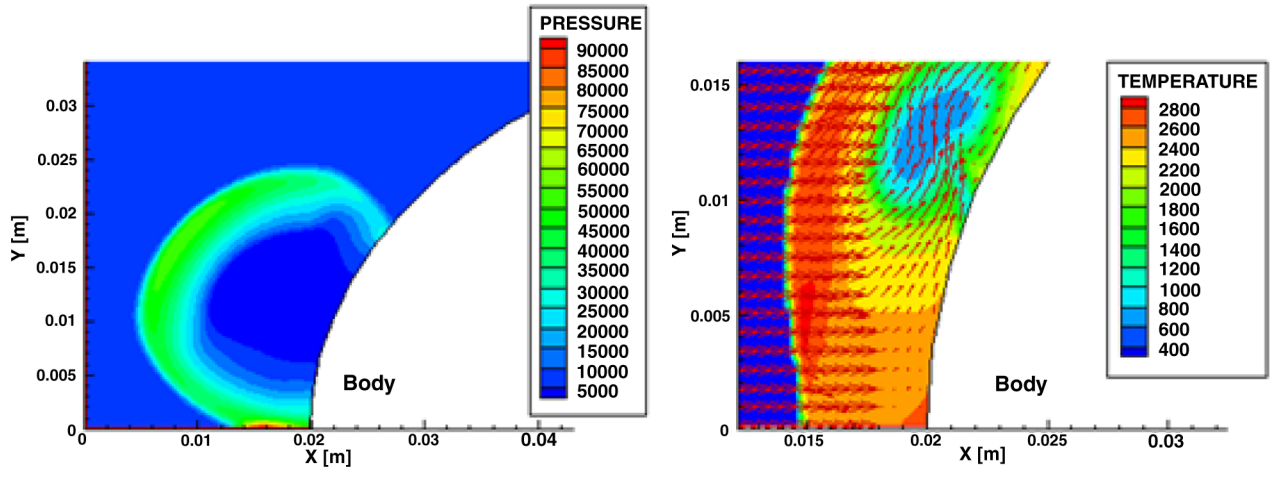

Fig. 6 Flowfield near the stagnation point: a) pressure contours after plume injection over the body in still air and b) temperature contours along with the vector field at altitude of flight of 20 km at $t \sim 10$ μs.

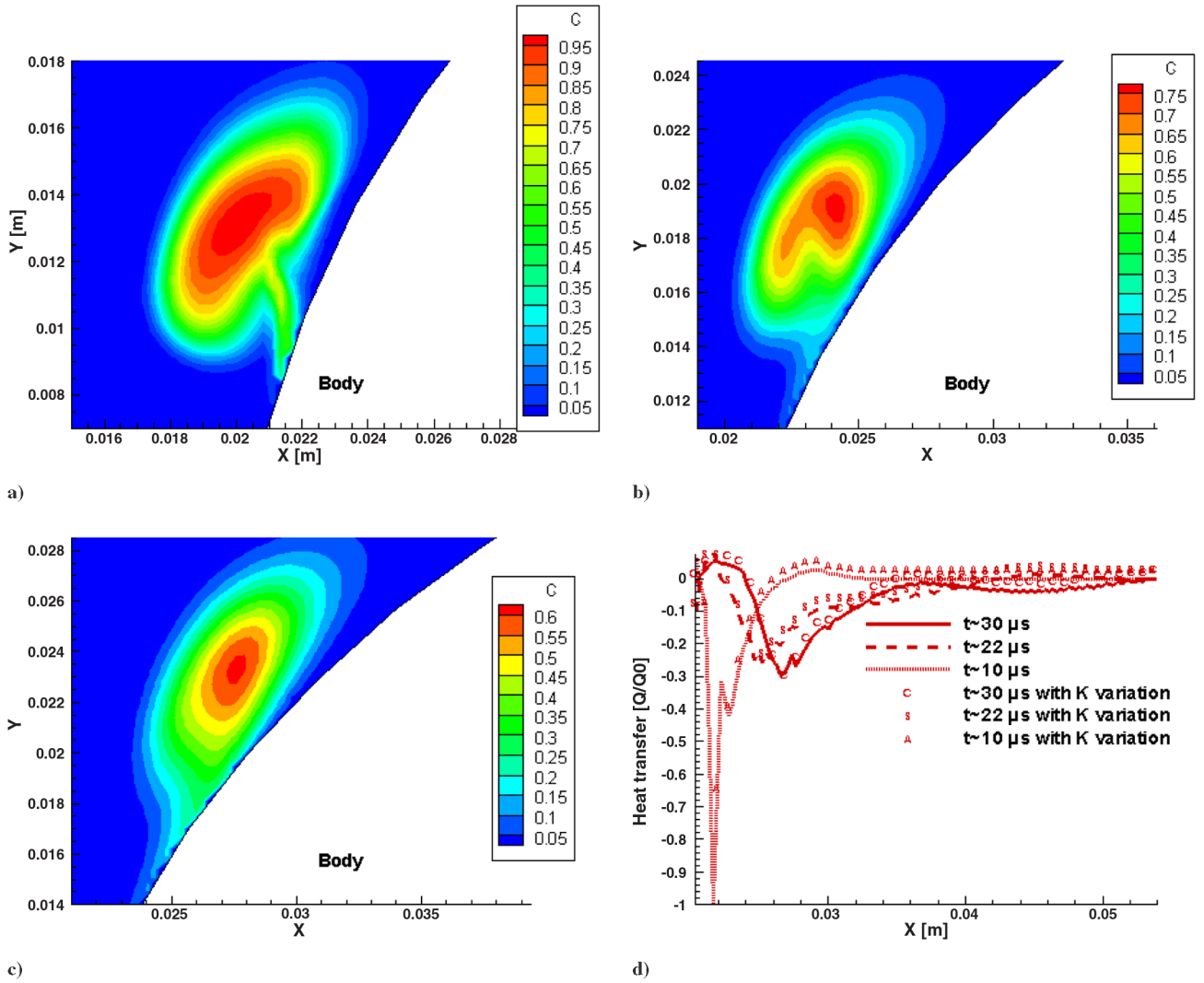

Fig. 7 Plume dynamics at the altitude of flight of 20 km: plume concentration at a) $t = 10$ μs, b) $t = 22$ μs, c) $t = 30$ μs, and d) heat transfer at the TPS surface with and without variation of thermal conductivity with temperature.

shock wave, as can be seen in Fig. 9a. This interaction of waves significantly affects the heat transfer.

For a longer time of plume evolution at the altitude of flight of 30 km, significant heating around the stagnation region of the body is observed. In Fig. 10, pressure contours and heat transfer for the corresponding time moments are shown. It can be observed in Fig. 10d that at the TPS surface, there are noticeable positive peaks (heating) that increase with time. This heating is caused by the shock wave associated with plume emergence. This shock wave interacts with the bow shock wave and reflects back on the TPS (see Figs. 10a–10c). In Fig. 10a, the bow shock wave is displaced momentarily due to this interaction and the reflection is smaller. Subsequently, at later time instants (Figs. 10b and 10c), the reflection and formation of secondary shocks are more pronounced, causing increased heating in the stagnation region.

In summary, at all altitudes, the temperature of the emerging plume gives the normalization coefficient for heat transfer, which corresponds to the maximum (cooling) heat transfer rate at that

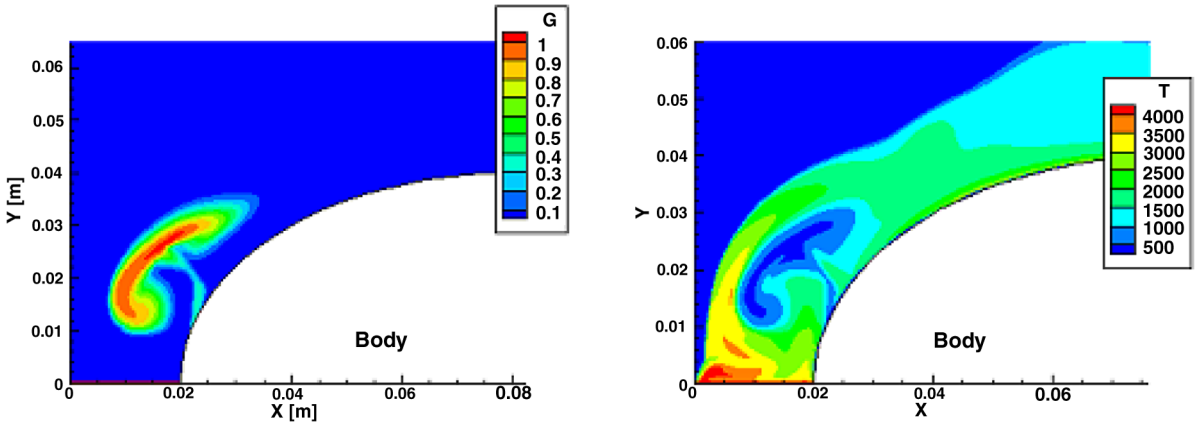

Fig. 8 Plume dynamics at the altitude of flight of 30 km at ($t \sim 25$ μs): a) plume concentration and b) temperature field.

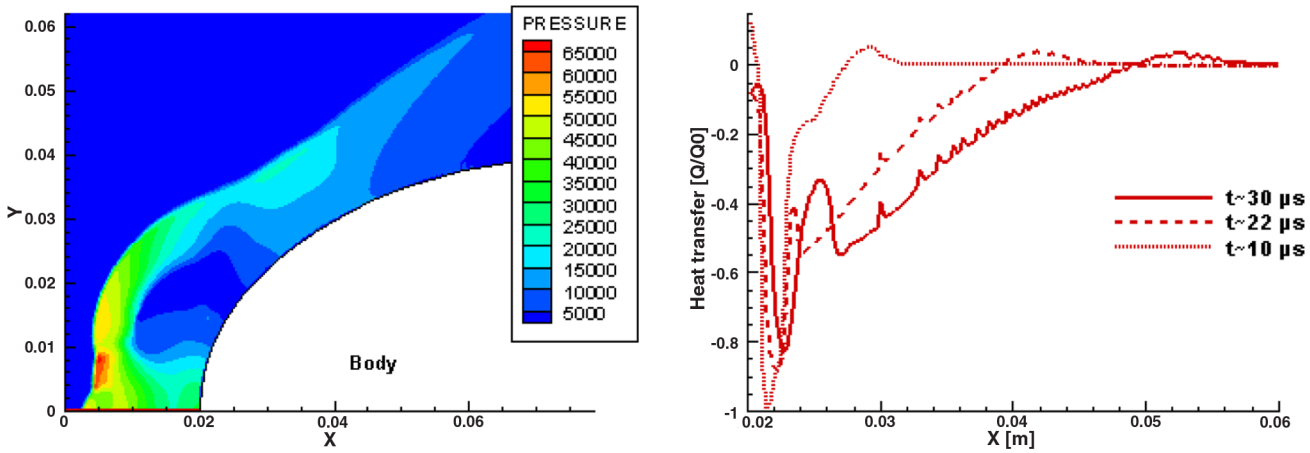

a) b)

Fig. 9 Interaction of waves and heat transfer at the altitude of flight of 30 km: a) pressure contours ($t \sim 22$ μs) and b) heat transfer at wall.

altitude. The intensity of cooling heat transfer along the TPS wall at later time moments is determined by the plume convection. The location of the maximum cooling effect is the farthest downstream for the flight at the altitude of 20 km and is associated with the tail of the plume. At ground level, the convection is relatively slow, whereas at the altitude of 30 km, the plume propagates farther in the direction perpendicular to the TPS wall, and the primary cooling is associated with one lobe of the kidney-shaped structure of the plume.

Apart from cooling, some heating effect is observed at all altitudes. Except at the ground level, this heating is caused by the outgoing pressure wave, due to the underexpanded plume injection. At the flight altitude of 20 km, this effect is modest around the stagnation region, whereas at the flight altitude of 30 km, the significant effect of this pressure wave is seen upstream and downstream of the plume over a significantly larger area of the TPS. At later time moments, the reflections of outgoing pressure wave cause significant heating at the

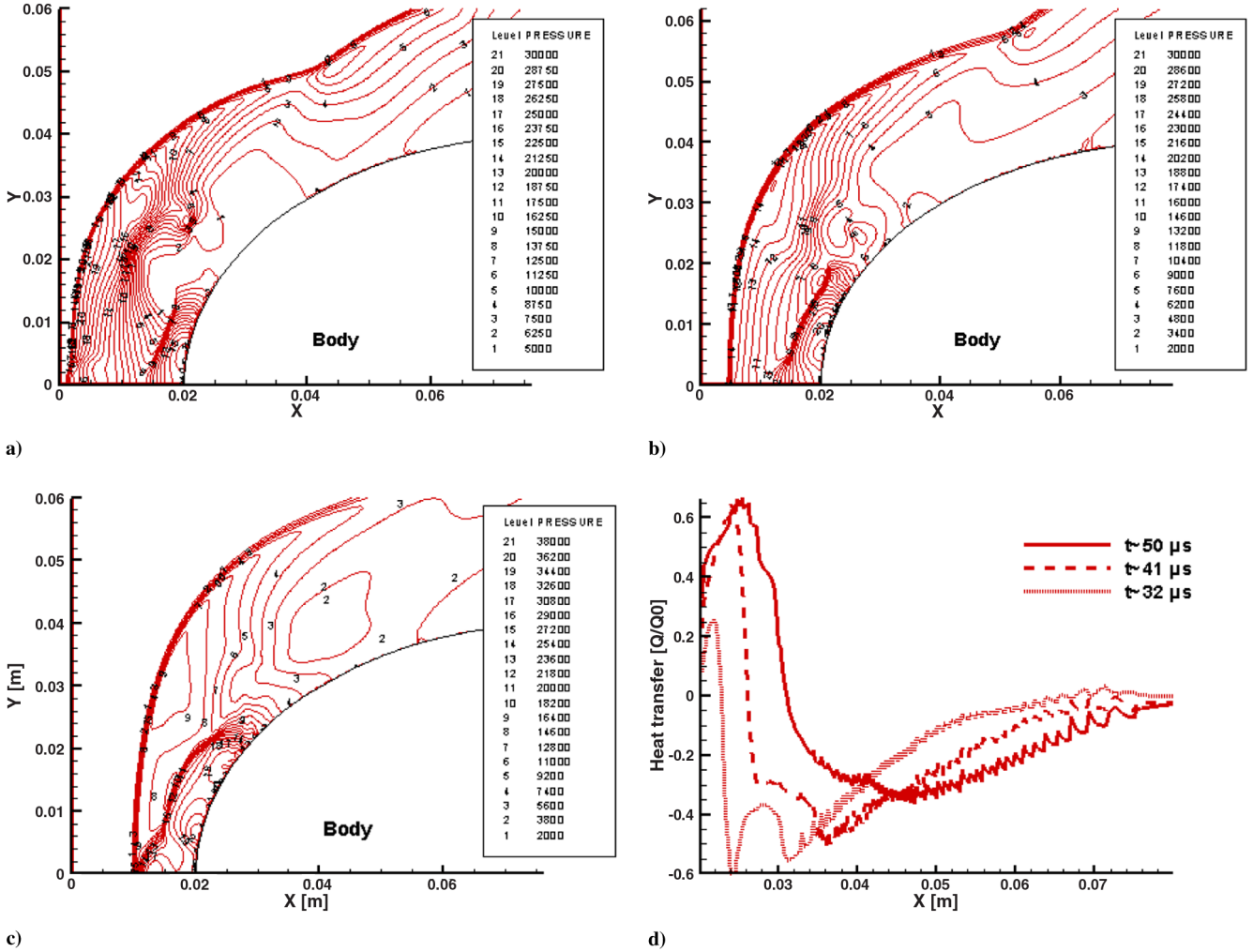

a) b) c) d)

Fig. 10 Formation of secondary shock waves: pressure contours at; a) $t \sim 32$ μs, b) $t \sim 41$ μs, c) $t \sim 50$ μs, and d) heat transfer at the TPS wall.

stagnation region. This heating becomes more significant than cooling, due to plume convection (see Fig. 10d).

IV. Heat Transfer for the Range of Plume Injection Pressures

The heat transfer for three different plume injection pressures (8, 16, and 24 atm) is shown in Fig. 11 at the flight altitude of 20 km. The initial temperature of the injected plume is the same for all considered cases. The heat transfer between the plume and the TPS appears to be different for these injection pressures. In Fig. 11, the normalization parameter Q_0 for all considered injection pressures is assumed to be equal to the value attained at $t \sim 10$ μs for the injection pressure of 24 atm. The maximum cooling heat transfer occurs at $t \sim 10$ μs for all injection pressures except for 16 atm, where the highest cooling location moves downstream, but peak values do not change significantly (in this case, the maximum is observed at $t \sim 22$ μs). The peak heat transfer is largest for 24 atm.

With increasing injection pressure, the plume propagates farther away from the TPS surface driven by its initial pressure. This is shown in the inset image of plume concentration in Fig. 11. For a higher injection pressure of 24 atm (see Fig. 11c), the plume core is separated from the TPS surface, thus reducing the heat convection. For 24 atm, the peak in heat transfer increases up to $t \sim 30$ μs, unlike for the smaller injection pressures, for which the peak decreases with time (see Figs. 11a and 11b). This increase in heat transfer is caused by the high-density plume that is pushed closer to the TPS surface by the recovering detached shock wave. For a low injection pressure of 8 atm, the rate of heat transfer decreases fast with time (see Fig. 11a). Compared with higher injection pressures, the plume has a lower level of concentration (see the inset image in Fig. 11a), indicating that the low-pressure plume mixes faster with the surroundings. The maximum heat transfer for an injection pressure of 16 atm is attained at $t \sim 22$ μs and the peak in heat transfer shows no significant change in time.

Overall, for a low injection pressure of the plume, the dynamics resemble those corresponding to the flight at ground level (see Sec. II.D). The plume is dragged along the TPS wall, the convection rate and convective speed of plume are relatively slow, and heat transfer diminishes faster than for larger injection pressures. For higher injection pressures, the plume convection can be more important for later time moments. For an intermediate plume injection pressure of 16 atm, the heat transfer rate is relatively steady in time. The magnitude of heat transfer is the largest for a high-pressure plume of 30 atm for all time moments.

V. Heat Transfer for Multiple Plume Injections

Ejection of multiple high-pressure underexpanded plumes may appear as a sequence of increasingly complex scenarios, including multiple plumes originating from the same location and multiple spatially distributed plumes caused by the complex topology of cracks at the TPS surface. The escape routes of pyrolysis gases may form cracks of different shapes. The typical size of cracks that appear because of intensive heating is of the order of submillimeters [27] to millimeters (see the view of a charring ablator with cracks after a test

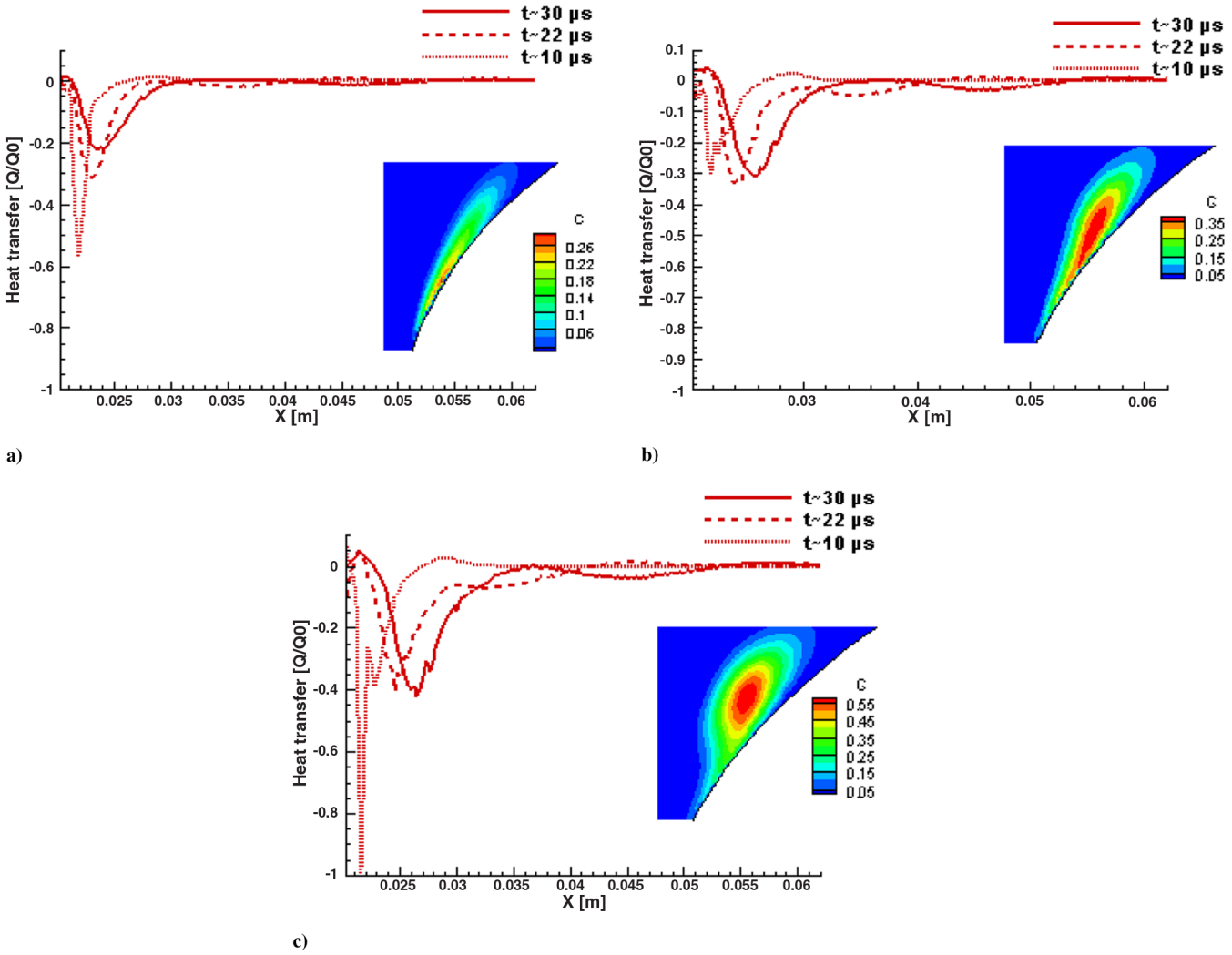

Fig. 11 Heat transfer with inset image of plume concentration at $t \sim 30$ μs for the range of initial plume injection pressures: a) 8 atm, b) 16 atm, and c) 24 atm.

in the VKI Plasmatron [8,9]). In these experimental photos, the cracks are long and narrow; that is, their length is much larger than their thickness. Therefore, the side 3-D effects that are typical for escape of plumes through round holes can be neglected in this study.

This section is focused on the interaction of plumes and interaction of pressure waves originating from the ejection of underexpanded plumes for a representative case of a pair of consecutively emerging plumes.

Figure 12 shows the plume pattern and heat transfer for two plumes when the second plume emerges at the tail of the first plume at $t = 35$ μs after emergence of the first plume. The TPS area in contact with the tail of the first plume may have the largest thermal stress because of the fast cooling that causes the formation of cracks and the emergence of the second plume. The normalization parameter Q_0 for heat transfer is the value obtained at $t \sim 10$ μs after the injection of the first plume (see Table 3). For later time moments, the peak in heat transfer is observed at the location of the tail of the new injected plume (see Fig. 12). These locations are $x \sim 0.035$ for $t \sim 50$ μs and $x \sim 0.04$ for $t \sim 60$ μs. For these time moments, the heat transfer is dominated by the second plume convection and its pattern is similar to that observed for a single plume. It should be noted, however, that the magnitude of peak cooling heat transfer is greater than unity for multiple plume injections, because the second plume emerges into the first cold plume. This shows that the intensity in heat transfer increases with new plume injections.

The positive heat transfer pattern upstream of the plume injection is qualitatively similar to that for the single plume injection. As discussed previously, these positive peaks were created by thepropagation of the plume pressure wave and its interaction withthe detached front shock wave. This pressure wave is able to heat upthe flow around the stagnation region (see Fig. 12d at $x \sim 0.02$ m).

VI. Heat Transfer for Different TPS shapes

The heat transfer and density contours for plume injection for two different body shapes of comparable size are shown in Fig. 13. In case A, the body is formed of a segment of an ellipse as in previous cases. In case B, the body is formed by a segment of a circle connected to a straight line making the angle of 10 deg, with the horizontal axis corresponding to the first test case in [17], and is typical of Earth reentry vehicles used for planetary missions.

The normalization parameter Q_0 for heat transfer is the value obtained at $t \sim 10$ μs for case B. It is observed that case B has higher heat transfer compared with case A. Peaks observed in both cases at $t \sim 22$ and 30 μs appear to be due to the convective heat transfer of the plume with the TPS. In case B, these peaks are observed for $x \sim 0.33$ and 0.041 m, whereas in case A, these peaks are observed for $x \sim 0.029$ and 0.033 m. This indicates that the plume travels faster in case B because of higher pressure and velocity gradients along the TPS surface that accelerate the plume. In case A, the flow is similar to that about the front portion of the sphere, whereas in case B, the flow similar to the impinging flow into the flat plate prevails at the front TPS surface.

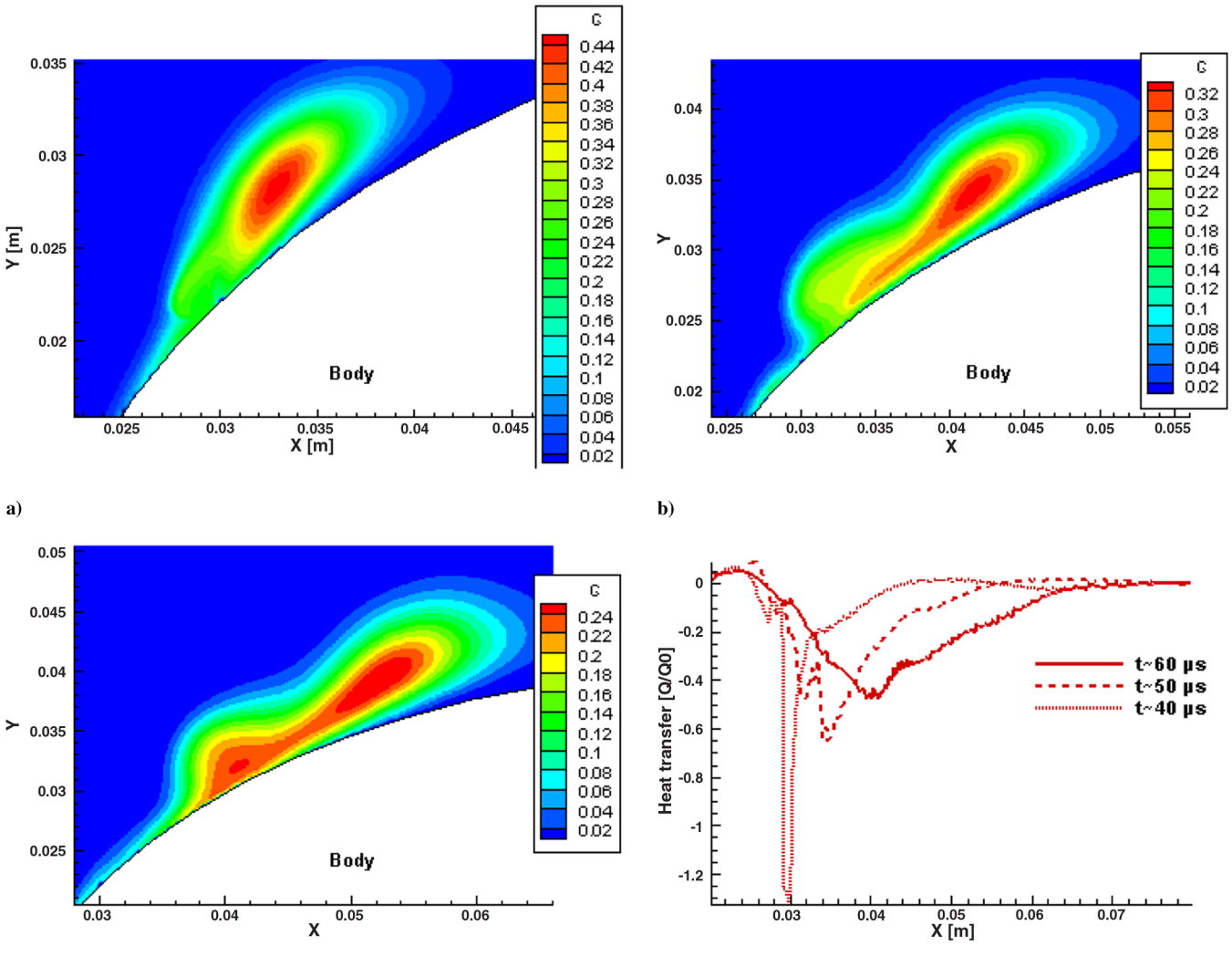

Fig. 12 Emergence of two consequent plumes at the flight altitude of 20 km. Concentration of plume material is shown at time moments a) $t \sim 40$ μs, b) $t \sim 50$ μs, and c) $t \sim 60$ μs, and d) heat transfer at the wall is shown.

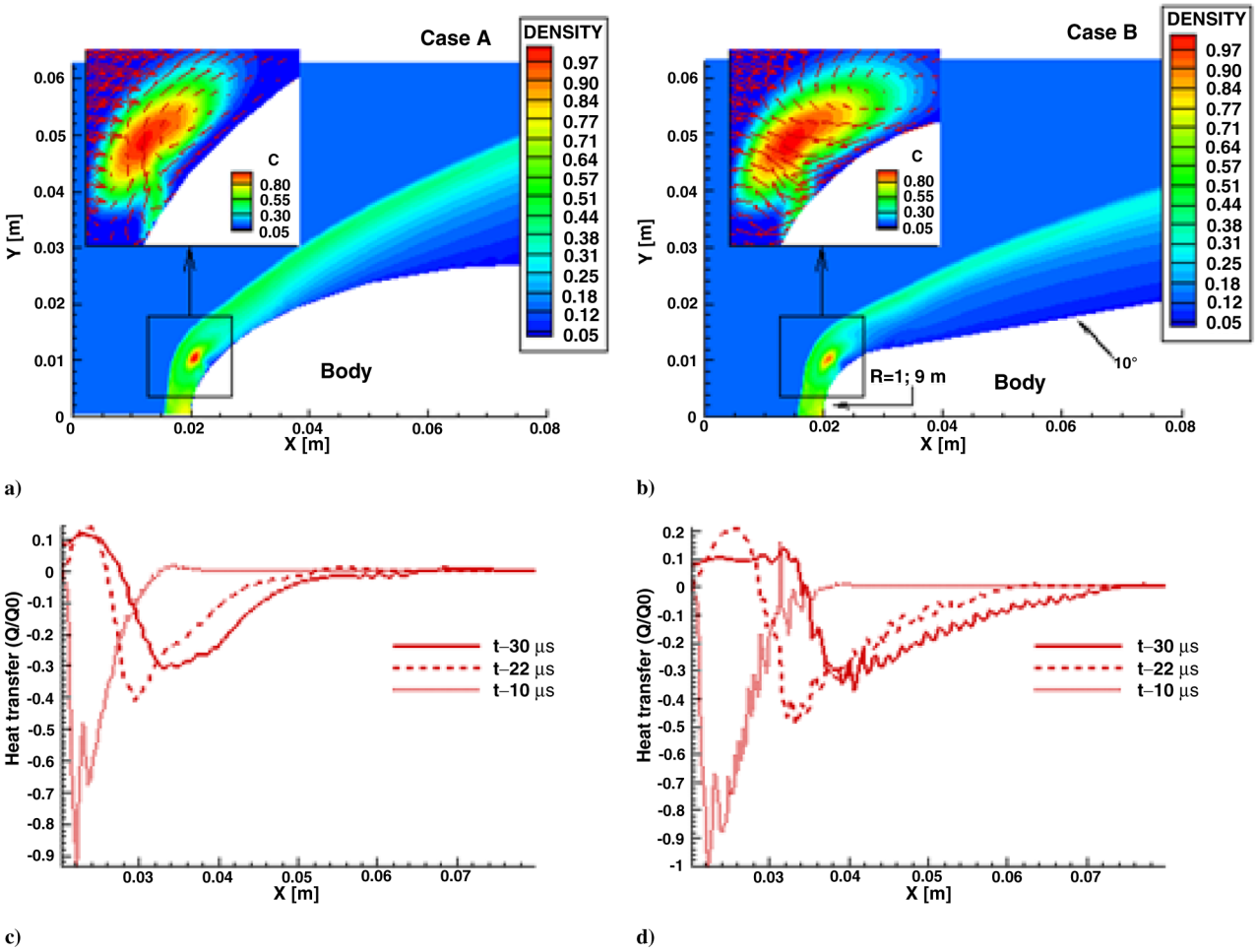

Fig. 13 Effect of TPS shape at the altitude of flight of 20 km: a–b) density contours at $t \sim 10$ μs with inset image showing plume concentration and modified velocity vector field and c–d) heat transfer at the TPS surface.

The plume patterns are shown in the inset image of Fig. 13. The vector field $\mathbf{V} - \mathbf{V}_{\text{ref}}$ is plotted to show the vortices by subtracting the velocity at a given point in the plume core for the respective plumes. It can be seen from the figure that the vortical structure is larger in case B, which causes more intense mixing. In both cases, positive heat transfer occurs upstream of the plume for $t \sim 22$ and 30 μs. This is due to the pressure wave associated with plume emergence. In case B, the strength of the front detached shock is lower than that in case A. The initial strength of the plume pressure wave is the same in both cases; consequently, this wave alters the flowfield to a larger degree in case B than in case A.

VII. Conclusions

Numerical simulations are performed to explore the effect of plumes formed through pyrolysis. The effects of initial plume ejection pressure, flight altitude, body shape, and emergence of multiple plumes are discussed. The altitude of the flight significantly affects the heat transfer between the emerging plume and the TPS. The pressure difference across the bow shock wave is higher for lower altitudes. At a high altitude of flight, the plume distorts the shock wave completely, and the flowfield behind the shock wave is changed significantly after the plume emergence. At a low altitude of flight, the pressure behind the shock wave is high enough that the plume is unable to eject away from the TPS surface and propagates along it. At a moderate altitude of 20 km, the plume distorts the shock wave temporarily, due to its interaction with the plume. For the given injection conditions of relatively cold pyrolysis gas, the simulation results show no significant difference between the plume patterns obtained by the Euler and Navier–Stokes equations.

The plume propagates the farthest distance along the TPS wall at moderate altitudes. Initially, a kidney-shaped structure is obtained, which then evolves into an oval shape and approaches the TPS wall after being pushed back by the recovering bow shock wave. Consequently, the maximum cooling by the plume tail occurs farther away from the stagnation point than with the low and high altitudes. At a high altitude of 30 km, the plume propagates farther away from the TPS and maintains its double-kidney shape. The cooling then occurs by interaction of one of the plume lobes with the TPS.

The cooling effect is larger for the high altitude of flight, because the temperature of the kidney-shaped plume remains cold. During the transformation of the plume from kidney shape to oval, its temperature rises and therefore the cooling effect is less for the moderate altitude of flight. Apart from cooling, some heating effect is observed at all altitudes. Except at the ground level, this heating is caused by the outgoing pressure wave, due to the underexpanded plume injection. At a moderate flight altitude of 20 km, this effect is significant around the stagnation region, whereas at higher flight altitudes, the effect of this pressure wave is seen upstream and downstream of the plume over a significantly larger area of the TPS. At a higher flight altitude of 30 km, the heating effect due to this wave is more pronounced than the cooling effect at later time moments.

The heat transfer is investigated for the range of initial injection pressure of the plume. Despite the fact that the plume is detached from the TPS for higher plume injection pressures, the heat transfer between the plume and the TPS is the most intense in this case. This is caused by the plume convection in later time moments when the plume is repelled by the bow shock wave toward the TPS.

For multiple plumes, it is observed that the emergence of the second plume increases the magnitude of heat transfer. The behavior of heat transfer for TPSs with different geometries but comparable

sizes shows that the heat transfer due to plume injection is lower for a body with a larger radius of curvature (i.e., with more smooth geometry). The heating effect due to the plume pressure wave is higher for a body that has a lower strength of the front detached shock.

Acknowledgments

Alex Povitsky and Kedar Pathak acknowledge partial support of the U.S. Air Force Office of Scientific Research through research grant FA9550-07-1-0457. Alex Povitsky thanks the U.S. Air Force Research Laboratory (Dayton, OH) for the Air Force Summer Faculty Fellowship from 2005–2008. The computations were conducted using Ohio Supercomputer Center facilities through a computer time grant to Alex Povitsky.

References

[1] Milos, F. S., and Chen, Y.-K., "Comprehensive Model for Multicomponent Ablation Thermochemistry," AIAA Paper 97-0141, Jan. 1997.

[2] Schneider, S. P., "Flight Data for Boundary-Layer Transition at Hypersonic and Supersonic Speeds," *Journal of Spacecraft and Rockets*, Vol. 36, No. 1, 1999, pp. 8–20. doi:10.2514/2.3428

[3] Komurasaki, K., and Candler, G. V., "Theoretical Consideration on Laminar-to-Turbulent Transitions over an Ablating Reentry Capsule," Inst. of Space and Astronautical Science, Rept. SP 17, Kanagawa, Japan, 2003, pp. 110–132.

[4] Bouilly, J.-M., Euzen, M., Labaste, V., Mignot, Y., and Gerrekens, P., "Design of Thermal Protection Systems for Reentry Vehicles. A Survey of Calculation and Characterization Techniques Used by Aerospatiale," *Space Technology*, Vol. 18, No. 3, 1998, pp. 99–108. doi:10.1016/S0892-9270(98)00013-X

[5] Yamada, T., Inatani, Y., Honda, M., and Hirai, K., "Development of Thermal Protection System of the MUSES-C /DASH Reentry Capsule," *Acta Astronautica*, Vol. 51, No. 1, 2002, pp. 63–72. doi:10.1016/S0094-5765(02)00054-1

[6] Berry, S. A., and Hamilton, H. H., "Discrete Roughness Effects on Shuttle Orbiter at Mach 6," AIAA Paper 2002-2744, June 2002.

[7] Ahn, H.-K., Park, C., and Sawada, K., "Response of Heatshield Material at Stagnation Point of Pioneer-Venus Probes," *Journal of Thermophysics and Heat Transfer*, Vol. 16, No. 3, 2002, pp. 432–439. doi:10.2514/2.6697

[8] Vancrayenest, B., "Investigation of the Thermochemistry of Ablation of Graphite for Planetary Entry Applications," Von Karman Inst. for Fluid Dynamics, Belgium, http://www.vki.ac.be/research/themes/survey2004pdf/ar13.pdf [retrieved 28 Apr. 2008].

[9] Vancrayenest, B., and Fletcher, D. G., "Investigation of the Thermochemistry of Ablation of Graphite for Planetary Entry Applications," AIAA Paper 2005-5062, June 2005.

[10] Duffa, G., Vignoles, G. L., Goyheneche, J.-M., and Aspa, Y., "Ablation of Carbon-Based Materials: Investigation of Roughness Setup from Heterogeneous Reactions," *International Journal of Heat and Mass Transfer*, Vol. 48, No. 16, July 2005, pp. 3387–3401. doi:10.1016/j.ijheatmasstransfer.2005.02.036

[11] Tang, S., Deng, J., Liu, W., and Yang, K., "Mechanical and Ablation Properties of 2D-Carbon/carbon Composites Pre-Infiltrated with a SiC Filler," *Carbon*, Vol. 44, No. 14, Nov. 2006, pp. 2877–2882. doi:10.1016/j.carbon.2006.06.003

[12] Aspa, Y., "Identification of Microscale Ablative Properties of C/C Composites Using Inverse Simulation," AIAA Paper 2006-2911, June 2006.

[13] Grujicic, M., Zhao, C. L., Dusel, E. C., Morgan, D. R., Miller, R. S., and Beasley, D. E., "Computational Analysis of the Thermal Conductivity of the Carbon–Carbon Composite Materials," *Journal of Material Science and Technology (Sofia)*, Vol. 41, No. 24, Dec. 2006, pp. 8244–8256. doi:10.1007/s10853-006-1003-x

[14] "Report of Columbia Accident Investigation Board Report, Volume I," NASA, Aug. 2003, http://www.nasa.gov/columbia/home/CAIB_Vol1.html [retrieved 28 Apr. 2008].

[15] Mullenix, N., and Povitsky, A., "Exploration of Pulse Timing for Multiple Laser Hits within a Combined Heat Transfer, Phase Change, and Gas Dynamics Model for Laser Ablation," *Applied Surface Science*, Vol. 253, No. 15, 2007, pp. 6366–6371. doi:10.1016/j.apsusc.2007.01.039

[16] Lobao, D., and Povitsky, A., "Interaction of Plume with Shock Waves in Laser Ablation," *AIAA Journal*, Vol. 43, No. 3, 2005, pp. 595–608. doi:10.2514/1.4388;also AIAA Paper 2003-3923.

[17] Chen, Y.-K., and Milos, F. S., "Finite-Rate Ablation Boundary Conditions for a Carbon-Phenolic Heat-Shield," AIAA Paper 2004-2270, July 2004.

[18] Zinovik, I., and Povitsky, A., "Modeling of Vapor-Droplet Plumes Ablated from Multiple Spots," *Applied Surface Science*, Vol. 253, No. 15, May 2007, pp. 6371–6376. doi:10.1016/j.apsusc.2007.01.038

[19] Zinovik, I., and Povitsky, A., "Dynamics of Multiple Plumes in Laser Ablation: Modeling of the Shielding Effect," *Journal of Applied Physics*, Vol. 100, No. 024911, 2006. doi:10.1063/1.2217108

[20] Quirk, J. J., and Karni, S., "On the Dynamics of a Shock-Bubble Interaction," *Journal of Fluid Mechanics*, Vol. 318, 1996, pp. 129–163. doi:10.1017/S0022112096007069

[21] Marble, F. E., "Dynamics of Dusty Gases," *Annual Review of Fluid Mechanics*, Vol. 2, Jan. 1970, pp. 397–446. doi:10.1146/annurev.fl.02.010170.002145

[22] Pathak, K., and Povitsky, A., "Inviscid, Viscous and Turbulent Models of Plume Dynamics for Laser Ablation of Carbon," *Journal of Computational and Theoretical Nanoscience*, Vol. 3, No. 4, 2006, pp. 565–578. doi:10.1166/jctn.2006.012

[23] Pathak, K., and Povitsky, A., "Modeling of Plume Dynamics with Shielding in Laser Ablation of Carbon," *Applied Surface Science*, Vol. 253, No. 15, May 2007, pp. 6359–6365. doi:10.1016/j.apsusc.2007.01.055

[24] *SFPE Handbook of Fire Protection Engineering*, 2nd ed., National Fire Protection Association, Quincy, MA, and Society of Fire Protection Engineers, Boston, 1995.

[25] Lemmon, E. W., and Jacobsen, R. T., "Viscosity and Thermal Conductivity Equations for Nitrogen, Oxygen, Argon, and Air," *International Journal of Thermophysics*, Vol. 25, No. 1, 2004, pp. 21–69. doi:10.1023/B:IJOT.0000022327.04529.f3

[26] Dec, J. A., and Braun, R. D., "An Approximate Ablative Thermal Protection System Sizing Tool for Entry System Design," AIAA Paper 2006-780, 2006.

[27] Jacobson, N. S., Calomino, A. M., and Webster, N., "As-Fabricated Reinforced Carbon/Carbon Characterized, in Research and Technology 2004," NASA TM-2005-213419, 2004, pp. 60–61.

C. Kaplan
Associate Editor